solids

MDPI

Article

Unveiling the Doping- and Temperature-Dependent Properties of Organic Semiconductor Orthorhombic Rubrene from First Principles

Israel Oluwatobi Olowookere [1], Paul Olufunso Adebambo [1,†], Ridwan Olamide Agbaoye [2,†], Abdulrafiu Tunde Raji [3,†], Mopelola Abidemi Idowu [4,†], Stephane Kenmoe [5,*,†] and Gboyega Augustine Adebayo [1,†]

[1] Department of Physics, Federal University of Agriculture, Abeokuta 111101, Ogun, Nigeria; israel.olowookere@gmail.com (I.O.O.); adebambopo@funaab.edu.ng (P.O.A.); adebayo@physics.unaab.edu.ng (G.A.A.)
[2] Department of Physics, Federal College of Dental Technology and Therapy, Enugu 400281, Enugu, Nigeria; agbaoye@physics.unaab.edu.ng
[3] Department of Physics, College of Science, Engineering and Technology (CSET), University of South Africa (UNISA), Pretoria 610101, South Africa; tunderaji@gmail.com
[4] Department of Chemistry, Federal University of Agriculture, Alabata, Abeokuta 111101, Ogun, Nigeria; maidowu408@yahoo.com
[5] Department of Theoretical Chemistry, University of Duisburg-Essen, Universitätsstr. 2, D-45141 Essen, Germany
* Correspondence: stephane.kenmoe@uni-due.de
† These authors contributed equally to this work.

Abstract: Due to its large hole mobility, organic rubrene ($C_{42}H_{28}$) has attracted research questions regarding its applications in electronic devices. In this work, extensive first-principles calculations are performed to predict some temperature- and doping-dependent properties of organic semiconductor rubrene. We use density functional theory (DFT) to investigate the electronic structure, elastic and transport properties of the orthorhombic phase of the rubrene compound. The calculated band structure shows that the orthorhombic phase has a direct bandgap of 1.26 eV. From the Vickers hardness (1.080 GPa), our calculations show that orthorhombic rubrene is not a super hard material and can find useful application as a flexible semiconductor. The calculated transport inverse effective mass and electronic fitness function show that the orthorhombic rubrene crystal structure is a p-type thermoelectric material at high temperatures.

Keywords: electronic structure; DFT; thermoelectric; organic semiconductor rubrene; transport properties

check for updates

Citation: Olowookere, I.O.; Adebambo, P.O.; Agbaoye, R.O.; Raji, A.T.; Idowu, M.A.; Kenmoe, S.; Adebayo, G.A. Unveiling the Doping- and Temperature-Dependent Properties of Organic Semiconductor Orthorhombic Rubrene from First Principles. *Solids* **2024**, *5*, 278–291. https://doi.org/10.3390/solids5020018

Academic Editor: Michael Reshchikov

Received: 24 March 2024
Revised: 29 April 2024
Accepted: 24 May 2024
Published: 29 May 2024

1. Introduction

Organic semiconductors (OSs) contain pi-bonded molecules which are made up of carbon and hydrogen atoms [1] and are bound together by van der Waals interactions. Therefore, OSs have much lower hole mobility than inorganic semiconductors due to significantly reduced covalent coupling generated by the van der Waals contact [2]. Nevertheless, interest and research in OS have grown in recent years. They are seen as potential candidates for the future generation of electronic gadgets, as they offer the possibility to be used for the manufacturing of low-cost and lightweight devices that may be huge in size and flexible [3]. The OS earliest application as a photo-conductive coating in laser printers [4] paved the way for other successful opto-electronic devices, such as Organic Solar Cells (OSCs) and Organic Light-Emitting Diodes (OLEDs) [5]. Due to their improved transport properties [6], OSs may soon substitute inorganic semiconductors as the primary material for high-speed electronics [6] devices. Graphene is an excellent example for its

potential to replace inorganic semiconductors such as silicon and gallium arsenide in the near future [7,8].

In spite of their promising future, there is still room for improvement in the characterization of OS regarding their rational design and the optimization of their properties. These properties are completely determined by the content and arrangements of the molecules making up the OS. This stems from the fact that these molecules are experimentally created via synthetic chemistry. OSs have an extremely low dielectric constant of approximately 3–5 [6]. This yields a large exciton binding energy and, most often, poor electrical characteristics. Nevertheless, recent breakthroughs have enabled to overcome many of the obstacles, providing new fundamental insight into the main factors governing the performance of OS [6].

Despite their low mobility, OSs still find application in OLEDs and solar cells. OLEDs are now widely employed in commercial displays [9]. They benefit from having high contrast, brightness, and lower power usage. As mentioned earlier, despite the limited mobility and high exciton binding energy, OS are also used in OLED televisions and smartphone displays [10]. These characteristics make OS more appropriate for emissive devices than absorptive ones. The OS are primarily electrical insulators that can become semiconductors when charges are introduced from the valence to conduction band through photo-excitation or doping [11]. In some cases, OSs exist as amorphous thin films or molecular solids [12]. Due to its remarkable charge carrier mobility and luminous efficiency [13], rubrene $C_{42}H_{28}$ (5,6,11,12-tetraphenylnaphthacene) is also a typical OS material that is useful in Organic Thin-Film Transistors (OTFTs), OLEDs and OSCs. Rubrene is also commonly used in OLEDs as yellow fluorescent dye to boost luminous efficiency, stability, and durability [14].

The rubrene structure is essentially a four-winged tetracene molecule [15] which belongs to the polycyclic aromatic hydrocarbon family. Organic molecular crystals are potential semiconductor materials for LEDs, solar cells, and electrical applications. Organic crystals differ from inorganic solids with covalent or ionic bondings in terms of mobility and photo-excitement due to weak intermolecular interactions [16]. Rubrene has the highest carrier mobility for holes 40 $cm^2/(V{\cdot}s)$ and a high photoconductivity, which make it an exceptional OS [17]. These properties are employed in applications of rubrene in luminous and flexible devices. Rubrene crystals have closed molecular packing that is oriented in a certain direction which is known as the "b" direction; this implies that transport in a rubrene crystal is one-dimensional in nature [18]. Growing high-crystalline rubrene thin films is expensive, and this impedes its practical applications [19]. Several techniques have been developed over the years to grow rubrene thin films. Rubrene thin films can be grown in amorphous, polycrystalline, or single-crystal forms, utilizing various techniques. Some of the experimental techniques include pulsed laser evaporation of solidified solutions [20] and physical vapor transport [21].

In recent years, the increase in demand for new innovations in electronics has grown rapidly, hence the need to investigate the elastic, mechanical, and temperature- and doping-dependent properties of OS rubrene. These findings will enable the creation of entirely new design rules with improved durability and precise parameter control.

Therefore, for the first time, we attempt to calculate and investigate the temperature- and doping-dependent properties of orthorombic rubrene using density functional theory (DFT) calculations. In this research, we represent the structural, electronic, elastic and mechanical (elastic constants, shear, bulk and Young modulus, Pugh's ratio and Vickers hardness) properties. Also, we intend to record the values for Pugh's ratio and Vickers hardness for the first time.

2. Method and Computational Procedure

Structural optimization of the initial atomic positions and lattice structure of orthorhombic rubrene were performed after obtaining the initial parameters from the study of Reyes-Martinez [22]. The electronic cutoff for wavefunctions, the Monkhorst–Pack k-point grid [23], and the lattice parameters optimization were carried out with a convergence crite-

ria of 1 mRy per atom. The structural optimization and electronic structure were carried out with the Perdew–Burke–Enzenhoff [24–26] exchange correlation functional of the density functional theory, DFT [27,28] as implemented in the Quantum Espresso Package [29,30] using a plane–wave cut-off of 45 Ry, and a 2 × 6 × 4 Monkhorst-Pack grid with a Gaussian broadening of 0.01 Ry. The thermo_pw code across a strain range of −0.0075 to +0.0075 at 0.005 steps was used to calculate the elastic constants using the stress–strain technique. Ultrasoft pseudopotentials [31] as obtained from QE Pslibrary [32] were used to treat the valence and core electrons interactions. To calculate the elastic properties of orthorhombic rubrene via the stress–strain method, the stiffness matrix Cij corresponding to nine independent elastic constants was obtained for the rubrene crystal structure with Laue class D_2h (mmm), while ions were relaxed in each deformation. Furthermore, the mechanical properties of rubrene were obtained from the elastic constants, such as the internal strain and load deflection [33]. The elastic constants were evaluated for small strains ($\in$) by applying Hooke's law and its energy E.

In the determination of the transport properties, a plane–wave calculation was performed to relax the system followed by a non-self consistence calculation with a dense 40,000 k-points. In the G vectors, 311,243 dense grids were used in the Fast Fourier Transform dimensions, while the starting wave functions were randomized with 784 atomic wave functions. The results obtained from the Boltztrap calculations were then used to obtain the transport effective mass, and the electronic fitness function through the TransM code [34]. These calculations help screen semiconductors as either thermoelectrics or in relation to conductivity.

3. Results and Discussion

3.1. Structural Properties of Orthorhombic Rubrene

As shown in Table 1, a lattice constant of 26.79 Å (50.8257 a.u.) was obtained and it is in good agreement with the experimental value of Ref. [22]. Table 1 shows the optimized lattice parameters a = 26.7903 Å, b = 7.1700 Å, and c = 14.2112 Å for orthorhombic rubrene at $\alpha = \beta = \gamma = 90°$. These values are in close agreement with those reported in theoretical and experimental studies [35–38].

Table 1. Calculated and measured lattice constant of orthorhombic rubrene.

Reference	Lattice Constants			Method/Theory
	a (Å)	b (Å)	c (Å)	
Present work	26.7903	7.1700	14.2112	GGA
Ref. [36]	26.86	7.19	14.43	GGA
Ref. [38]	26.660	7.142	14.025	vdw-DFT
Ref. [38]	26.965	7.206	14.442	Experiment at 294 K
Ref. [35]	26.789	7.170	14.211	Experiment at 100 K
Ref. [22]	26.79	7.17	14.24	Experiment
Ref. [37]	26.7450	7.1455	14.1289	GGA

The relaxed structure of orthorhombic rubrene (Figure 1b) shows the compound to be a polymorph with the Cmca space group. Whenever rubrene molecules unite to form orthorhombic crystals, the resulting molecules have a centrosymmetric structure with 2/m symmetry. The cell parameters of orthorhombic rubrene crystal (as reported in Table 1) show that the molecules are organized in a herringbone packing pattern with nearly complete π–π stacking in the b direction. This is responsible for its large charge-carrier mobility, which has been affirmed in several pieces of research [18,38]. The mobility of charge carriers in orthorhombic monocrystals can approach 40 $cm^2/(V\cdot s)$, which is equivalent to that of amorphous silicon [39,40]. As seen in most organic crystals, rubrene's electronic transport is very anisotropic. High mobility values can only be obtained along the lattice's b axis. The features obtained from Figure 1b agrees reasonably well with the

results of Refs. [38,41]. The structural properties obtained in this work agree with previous theoretical and experimental values.

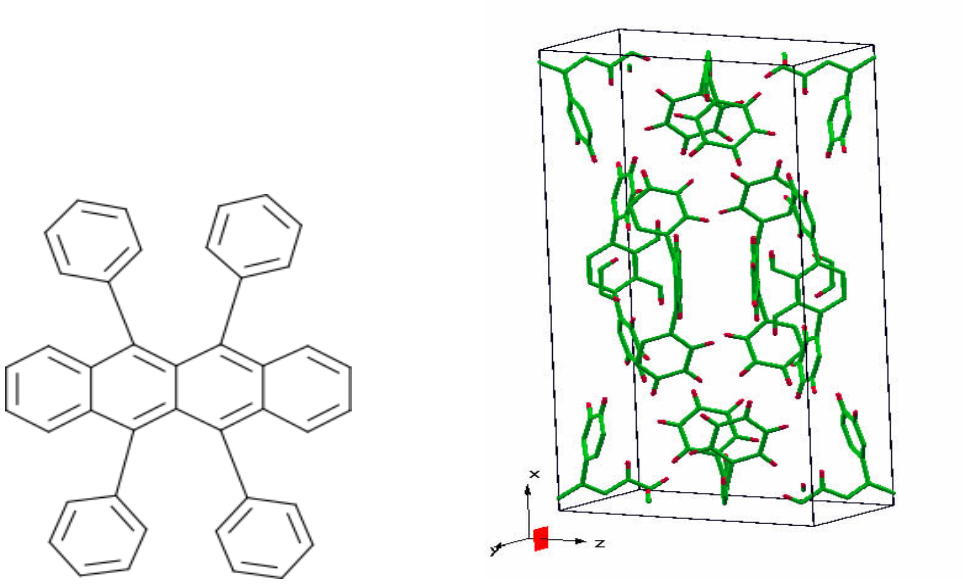

(**a**) (**b**)

Figure 1. Molecular and crystal structure of OS rubrene.

3.2. Electronic Properties

Figure 2 depicts the density of the state and band structure, as well as the state and behavior of electrons in an orthorhombic rubrene crystal. The numerical value for the direct bandgap is shown in Table 2. Generally, an energetic bandgap of ∼1–5 eV is recorded for OSs such as orthorhombic rubrene [36], as they tend to have a diminishing density of states around the Fermi energy. This is proportional to the size of the electrical gap, which is fairly considerable. This reduces the density of thermally generated charge carriers in pure organic crystals, with respect to silicon.

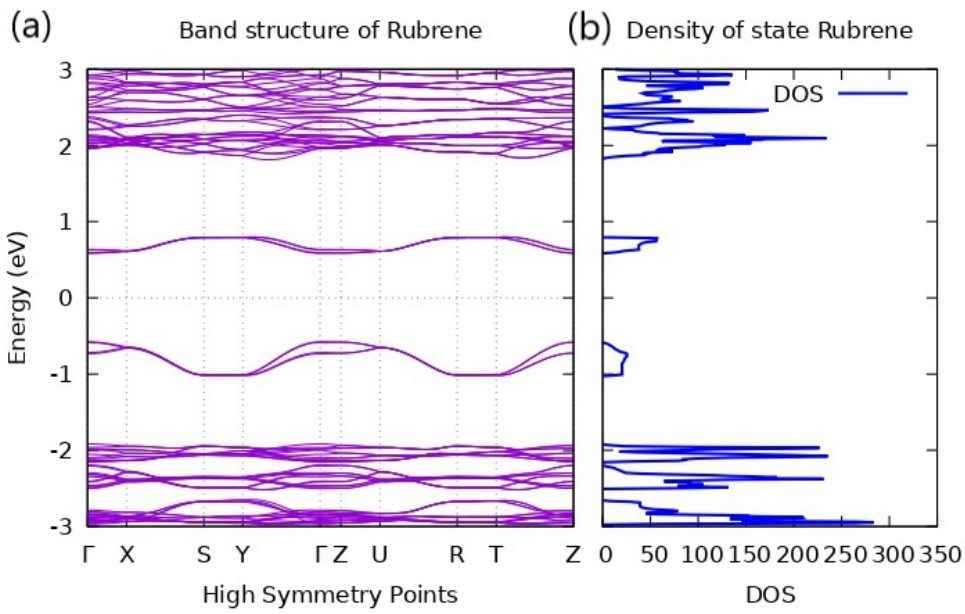

Figure 2. (**a**) Band structure of orthorhombic rubrene. (**b**) Density of states of orthorhombic rubrene.

Table 2. Comparison of bandgaps (HOMO-LUMO) of orthorhombic rubrene obtained in this work, experiments and previous calculations.

Reference	Bandgap		Theory
	Nature	Energy (ev)	
Present work	Direct	1.26	PBE
Ref. [37]	Direct	1.13	PBE
Ref. [42]	Direct	1.357	B3LYP 6-311G
Ref. [43]	Direct	2.50	B3LYP/6-311G(d,p)

As shown in the band structure (Figure 2), the bottom of the conduction band (CB) and the top of the valence band (VB) occur at the same momentum value. This implies that the band structure of OS rubrene has a direct bandgap as can be observed with some other OSs. The direct bandgap of 1.26 eV obtained within PBE agrees with the calculation of Ref. [37] using PBE also with a direct bandgap of 1.13 eV. Refs. [43,44] found a greater disparity between HOMO and LUMO. Their calculated bandgap is 2.50 eV and 2.60 eV, respectively, at the B3LYP/6-311G(d,p) level, which differs from other calculations. So far, there is no theoretical literature report on the consequential variation in the HOMO-LUMO gap [45]. The structural characteristic of the highest VB controls the hole transport behavior. The band splitting of the VB of orthorhombic rubrene is fairly minimal. Pressure increases intermolecular interaction, resulting in increased mobility [46]. High mobilities are only for holes, and electron mobilities are several orders of magnitude lower [44,47]. Rubrene is a p-type material, as are the vast majority of OSs [44].

The number of possible electrons (or hole) states per volume at a given energy is given by the density of states as shown in Figure 2b. The density of states distribution at the top of VB is relatively smooth in the orthorhombic rubrene.

Figure 3 shows the brillouin zone of orthorhombic rubrene within the high symmetry points. Figure 2a depicts the band structure along the k-path Γ – X – S – Y – Γ – Z – U – R – T – Z, where Γ – Z corresponds to the 'a' crystal axis and Γ – Y to the 'b' axis in real space [18].

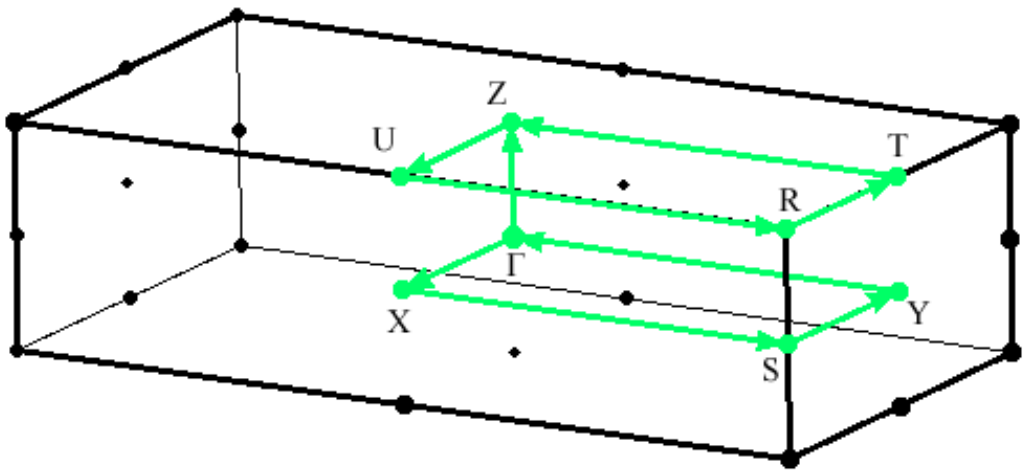

Figure 3. Brillouin zone of pristine orthorhombic rubrene within the high symmetry points.

3.3. Elastic Properties

The values of the computed C_{ij} show that the Born–Huang stability criteria have been fully satisfied [48], which proves rubrene to be mechanically stable. The independent elastic constants of orthorhombic rubrene is shown in Table 3. The estimated bulk modulus B, shear modulus G, Young's modulus E, Poisson ratio, Pugh ratio, and Vickers hardness using the Voigt–Reuss–Hill approximation are shown in Table 4 [49]. According to [50], a material is considered to be ductile if its bulk to shear modulus ratio B/G is more than 1.75; otherwise, it is brittle. The obtained Pugh ratio is 0.74667, which shows rubrene to be

more brittle than ductile. This property implies the ability to break with minimal elastic deformation when stressed and no considerable plastic deformation. Brittle materials have more strength than ductile materials. Brittle materials are more resistant to compression. Even high-strength brittle materials absorb relatively little energy before breakage. This feature proves the ability of orthorhombic rubrene as an OS that is useful in redefining the future of flexible and stretchable electronics. Furthermore, the Poisson's ratio can also prove the ductility of a material if the ratio is greater than 0.26 and brittleness is less than 0.26. The obtained Poisson ratio is 0.03292, which agrees with the Pugh ratio that we can classify orthorhombic rubrene as brittle.

Table 3. Comparison of independent elastic constants of orthorhombic rubrene obtained in this work, experiments, and previous calculations.

Reference	**This Work**	**Ref.** [22]	**Ref.** [38]	**Ref.** [38]
Method	PBE	AIREBO	vdw-DFT	Experiment
C_{11}(GPa)	18.8	15.54	25.31	18.48
C_{12}(GPa)	−8.7	1.08	6.94	2.63
C_{13}(GPa)	1.6	2.08	6.78	7.68
C_{22} (GPa)	13.6	17.85	16.99	13.39
C_{23} (GPa)	9.4	10.82	10.53	7.77
C_{33} (GPa)	14.6	13.29	13.94	14.32
C_{44} (GPa)	7.2	2.03	6.66	6.46
C_{55} (GPa)	13.2	1.97	4.41	2.8
C_{66} (GPa)	6.5	3.36	3.67	6.8

The Vickers hardness H_v is obtained as shown in Table 4. The hardness of a material measures its resistance to plastic deformation produced by applied forces. The result helps characterize the elastic and plastic properties of a solid. The predicted Vickers hardness H_v of 1.080 GPa was obtained for orthorhombic rubrene using Chen's model [51]. The result shows that orthorhombic rubrene is far from hard and cannot be classified as super hard.

$$\text{Elastic Constants } C_{ij} \text{ (GPa)} = \begin{bmatrix} 18.846944 & -8.738236 & 1.566589 & 0.00000 & 0.00000 & 0.00000 \\ -8.738236 & 13.633697 & 9.433130 & 0.00000 & 0.00000 & 0.00000 \\ 1.566589 & 9.433130 & 14.599899 & 0.00000 & 0.00000 & 0.00000 \\ 0.00000 & 0.00000 & 0.00000 & 7.220388 & 0.00000 & 0.00000 \\ 0.00000 & 0.00000 & 0.00000 & 0.00000 & 13.187243 & 0.00000 \\ 0.00000 & 0.00000 & 0.00000 & 0.00000 & 0.00000 & 6.507988 \end{bmatrix}$$

Calculated elasticity tensor for orthorhombic rubrene.

Also, the calculated reduced elastic constants and anisotropy ratio (C_{22}/C_{33}) of orthorhombic rubrene obtained in this work is shown in Table 5. The values of reduced constants C_{22}, C_{33}, and the anisotropy ratio (C_{22}/C_{33}) are in close agreement with the result of Ref. [38] from the experimental and vdw-DFT method. These findings may be beneficial not only for studying the strain effect on carrier mobility [18] but also for rubrene's actual use as a flexible electrical device [38].

Its directional elastic properties need to be analyzed and visualized to better understand an anisotropic material such as rubrene. This includes the Young modulus, linear compressibility, shear modulus, and Poisson ratio. The Debye temperature and average Debye sound velocity recorded in this research for orthorhombic rubrene are 331.008 K and 2384.484 m/s, respectively (Table 4).

Table 4. Calculated Voigt–Reuss–Hill approximation moduli for orthorhombic rubrene in this work.

Method	PBE
Bulk Modulus (GPa)	4.163
Shear Modulus (GPa)	11.519
Young Modulus (GPa)	5.576
Poisson Ratio	0.03292
Pugh Ratio (B/G)	0.74667
Vickers Hardness (GPa)	1.08
Average Debye sound velocity (m/s)	2384.484
Debye temperature (K)	331.008

Table 5. Calculated reduced elastic constants and anisotropy ratio (C_{22}/C_{33}) of orthorhombic rubrene obtained in this work, experiments, and previous calculations.

Reference	Method	C_{22} (GPa)	C_{33} (GPa)	Anisotropy Ratio (C_{22}/C_{33})
This work	PBE	13.6	14.6	0.93
[38]	vdw-DFT	15.08	12.12	1.24
[38]	Experiment	13.02	11.13	1.17

The Young modulus is a mechanical property that measures the tensile/rigidity or stiffness of a material when the force is applied. It implies the ratio of the tensile stress to the proportional deformation/tensile strain:

$$E = \frac{\sigma}{\varepsilon} \tag{1}$$

where tensile stress $\sigma = \frac{F}{A}$ is the force per unit area, and tensile strain $\varepsilon = \frac{dl}{l}$ is the extension per unit length. The Young modulus reported for orthorhombic rubrene in this work is 55.76 kbar, which shows rubrene as a non-rigid material (Figure 4a).

Linear compressibility, or the bulk modulus, helps describe a material's behavior when pressure is applied, which can be either negative or positive. The 2D and 3D surface plots (Figures 4b and 5b) show the directions corresponding to positive values of linear compressibility plotted in green and the negative value in red. The result indicates that orthorhombic rubrene crystal structure exhibits negative linear compressibility.

The shear modulus is the ratio of shear stress to the shear strain. It gives information on how resistant a material is to deformations as shown in Figures 4c and 5c. The 2D and 3D plots of the Poisson ratio in Figures 4d and 5d show the lateral strain and the longitudinal strain on orthorhombic rubrene. The Poisson ratio for elastic materials is the ratio of the lateral strain and longitudinal strain, which gives information on how materials deform under loading. However, the calculated Poisson ratio value is 0.03292, which lies between -1 and 0.5. The result shows the pristine form of orthorhombic rubrene as being almost perfectly incompressible, as there is little or no transverse deformation when axial strain is applied.

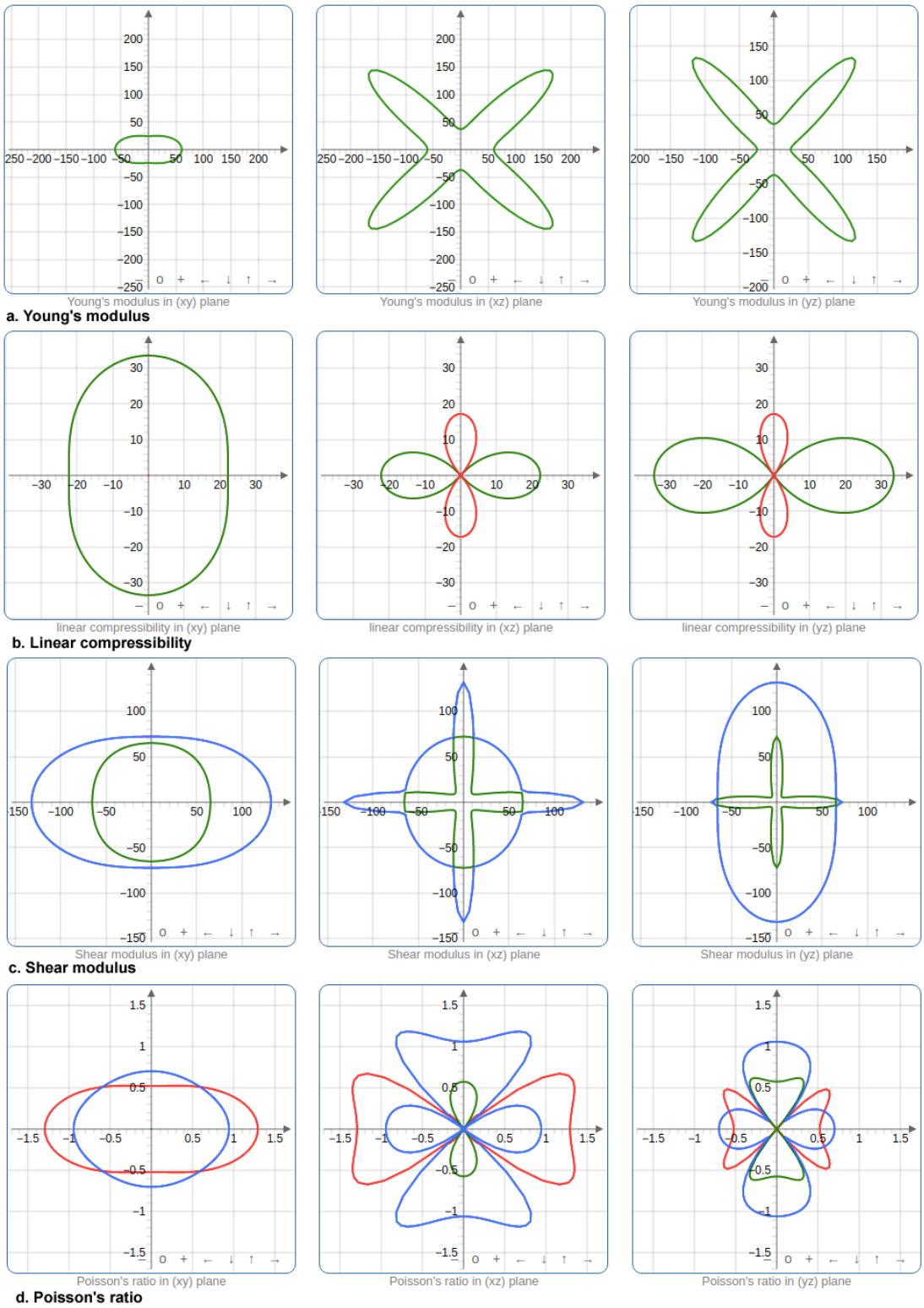

Figure 4. (**a**) Young's modulus, (**b**) linear compressibility, (**c**) shear modulus, and (**d**) Poisson ratio in 2D showing its directional planes.

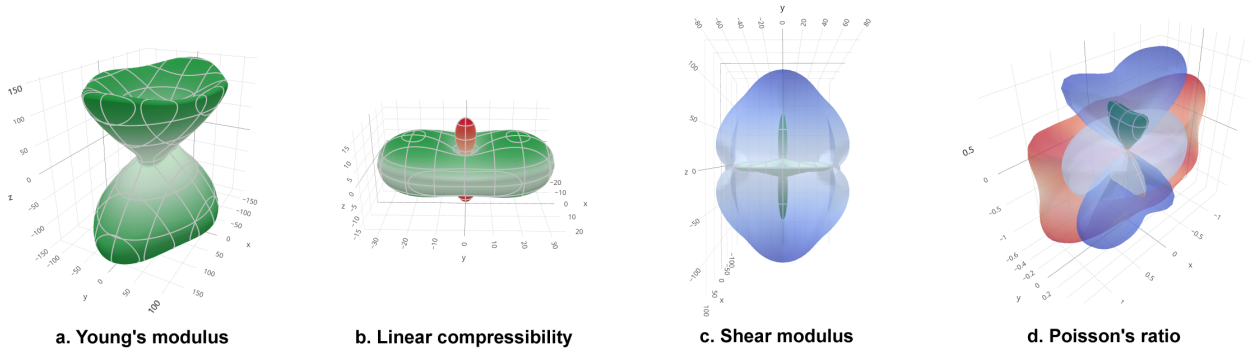

Figure 5. (**a**) Young's modulus, (**b**) linear compressibility, (**c**) shear modulus, and (**d**) Poisson ratio in 3D showing its directional planes.

3.4. Temperature- and Doping-Dependent Properties

To address the thermoelectric properties, the electronic fitness test is crucial, as it evaluates the thermopower for arbitrary band structures and conductivity [34]. Suitable thermoelectric materials, in general, have intricate electronic structures that are not described by a simple parabolic band [34]. Therefore, electronic fitness function calculation is necessary to identify such materials and address the σ (Conductivity) and S (Seebeck coefficient) conflict.

The electronic fitness function (EFF) displayed in Figure 6 shows an increase in temperature for n-p carrier concentrations, which is caused by the rising temperature and which improves its thermoelectric performance. There is a dip at carrier concentration 6.5×10^{21} for the hole concentration, and peaks are reached at 2×10^{21} and 1.1×10^{22}. This work also predicts that orthorhombic rubrene has a high electronic fitness function at about 500 K. OSs like rubrene are mostly p-type semiconductors.

The structure for the EFF in Figure 6 shows larger p-type EFF values at high carrier concentrations. This is attributed to the high anisotropic property of rubrene. Furthermore, as the temperature rises, it exhibits improved p-type performance. Valley anisotropy, higher band degeneracy, and multiband contributions in valence bands at higher energies, particularly at high doping levels, result in larger EFF in p-type materials. The features observed from these results show orthorhombic rubrene as a promising organic material for thermoelectric applications.

Figure 7 depicts the transport inverse effective mass as a function of carrier concentrations ranging from 300 K to 800 K. The result shows that it exhibits a light effective mass of holes. This agrees with the experiments performed in Ref. [52].

The power factor, electrical conductivity, and the Seebeck coefficient of rubrene are presented in Figure 8. This is shown with respect to temperature in the range of 300 to 800 K. Our power factor results show that the power factor increases as the temperature increases. Our results of the electrical conductivity and the Seebeck coefficient indicate that rubrene displays a promising thermoelectricity. In particular, the higher the Seebeck coefficient in any material, the better the efficiency of such material for thermoelectric properties. For rubrene, the highest and lowest values of the Seebeck coefficient are noted at room temperature, which implies that this material has a good thermoelectricity trait. The peak maximum for the p-type doping is found at 1800 $\mu V.K^{-1}$, while the minimum at n-type doping is found at -1300 $\mu V.K^{-1}$.

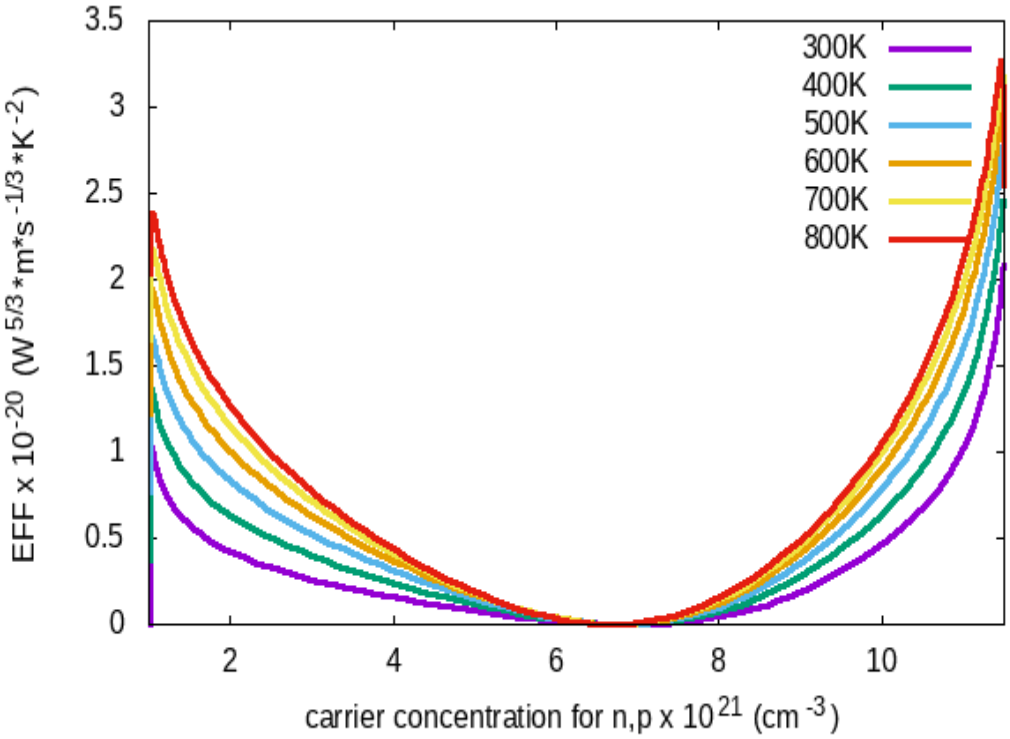

Figure 6. Electronic fitness function of rubrene against carrier concentrations from 300 K to 800 K.

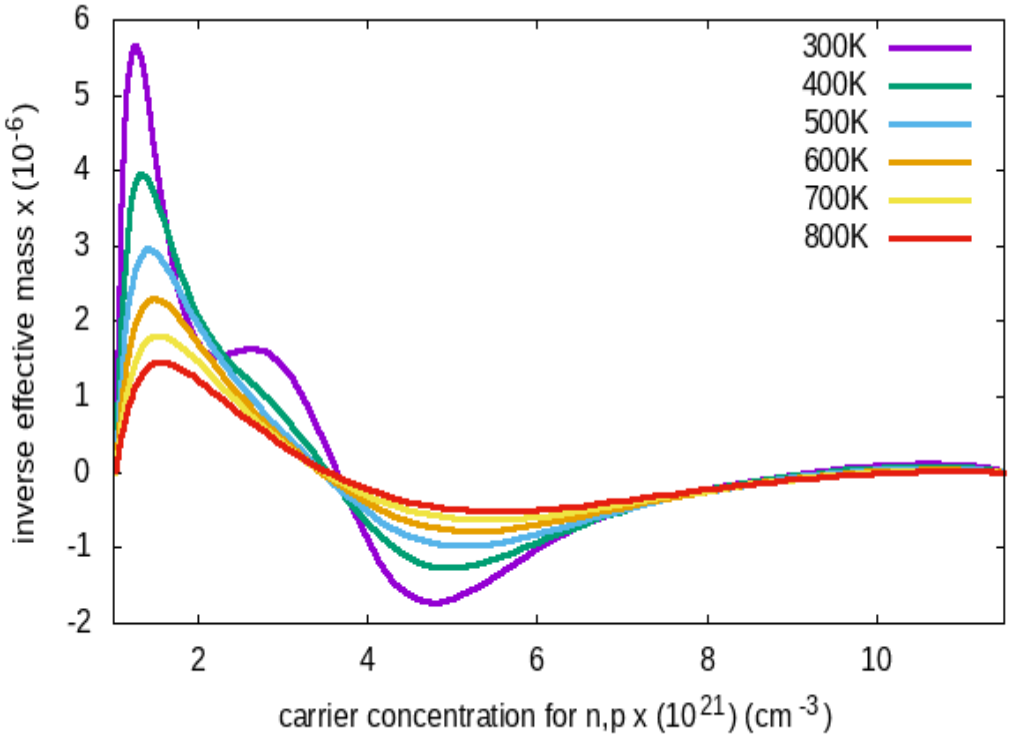

Figure 7. Inverse effective mass as a function of the carrier concentrations from 300 K to 800 K.

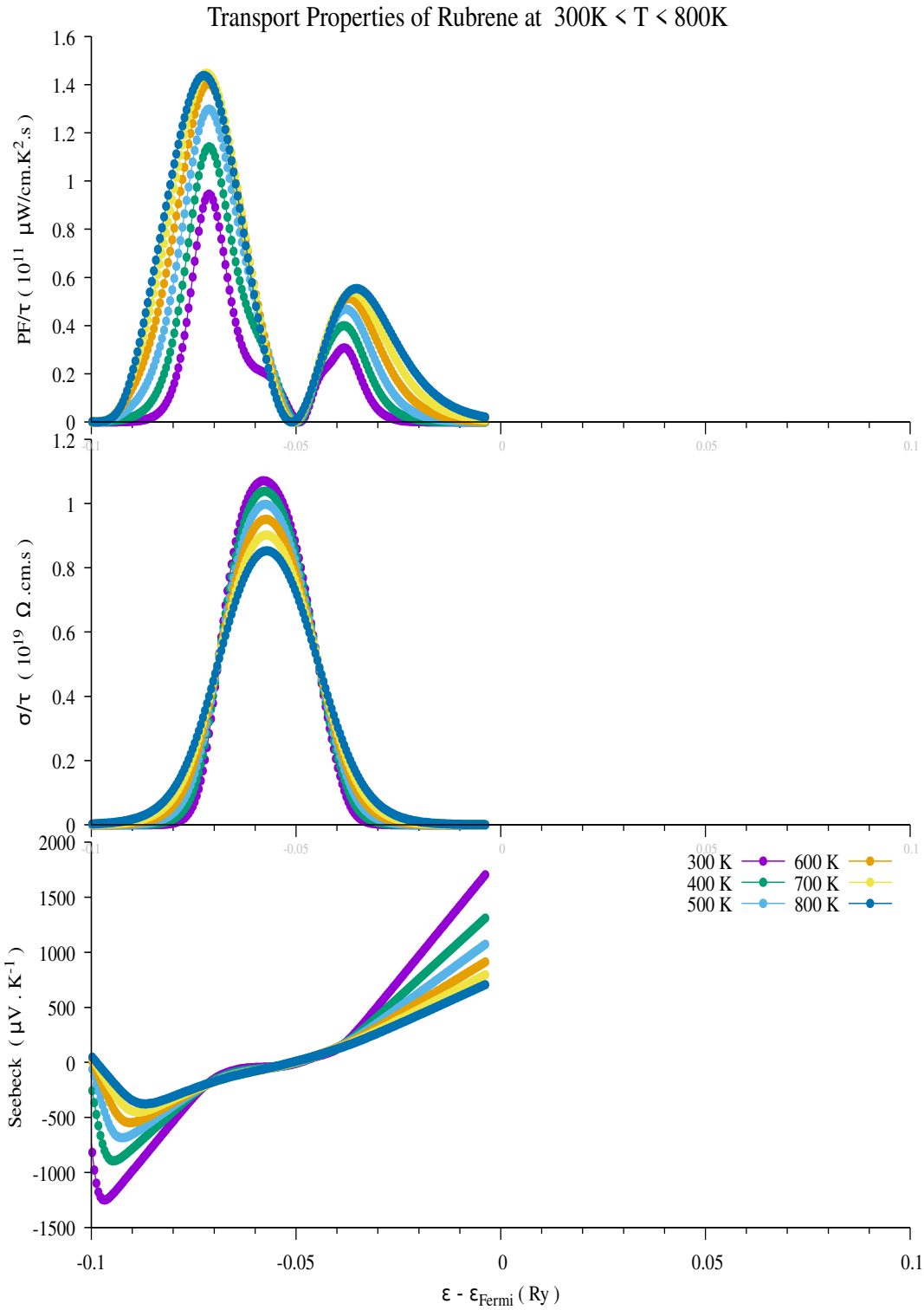

Figure 8. Transport properties of rubrene showing the power factor, electrical conductivity and Seebeck coefficient, respectively.

4. Conclusions

Using density functional theory via first-principles calculations, the structural, electrical, lattice dynamics, elastic, and temperature- and doping-dependent characteristics of orthorhombic rubrene are unveiled. Other properties, such as the Pugh ratio, Vickers

hardness, electronic fitness function, and transport effective mass of the orthorhombic rubrene crystal structure, are predicted in the present work.

The relaxed structure of orthorhombic rubrene shows that it has a high charge carrier mobility. The band structure calculations show that orthorhombic rubrene has a direct bandgap of 1.26 eV. This property makes it suitable for use in high-power electronics. The small bulk modulus (4.163 GPa) and Vickers hardness (1.080 GPa) reflect the orthorhombic rubrene crystal structure as not super hard. The obtained Pugh ratio is 0.74667, which shows rubrene to be brittle rather than ductile. The calculated transport inverse effective mass and electronic fitness function confirm the orthorhombic rubrene crystal structure to be a thermoelectric material of the p-type. Furthermore, the results of the transport effective mass and the electronic fitness function obtained show that rubrene is a promising thermoelectric material that performs best at high temperatures of about 500 K.

Author Contributions: Conceptualization, G.A.A.; methodology, P.O.A.; validation, G.A.A., P.O.A. and I.O.O.; investigation, I.O.O.; resources, A.T.R.; data curation, R.O.A.; writing—original draft preparation, review and editing, M.A.I.; supervision, S.K. and G.A.A.; project administration, G.A.A. All authors have read and agreed to the published version of the manuscript.

Funding: The APC was funded by Open Access Publication Fund of the University of Duisburg-Essen.

Data Availability Statement: The original contributions presented in the study are included in the article, further inquiries can be directed to the corresponding author.

Acknowledgments: The authors acknowledge computational time support from South Africa's Centre for High Performance Computing, CHPC, through collaboration with ATR.

Conflicts of Interest: The authors declare no conflicts of interest.

References

1. Jung, J.; Ulański, J. *Chapter 6. Charge Carrier Transport in Organic Semiconductor Composites—Models and Experimental Techniques*; John Wiley and Sons, Ltd.: Hoboken, NJ, USA, 2019; pp. 309–363. [CrossRef]
2. Ahmad, S. Organic semiconductors for device applications: Current trends and future prospects. *J. Polym. Eng.* **2014**, *34*, 279–338. [CrossRef]
3. Dey, A.; Singh, A.; Das, D.; Iyer, P. *Organic Semiconductors: A New Future of Nanodevices and Applications*; Springer: Cham, Switzerland, 2015; pp. 97–128. [CrossRef]
4. Diemer, P.J.; Harper, A.F.; Niazi, M.R.; Petty, A.J., II; Anthony, J.E.; Amassian, A.; Jurchescu, O.D. Laser-printed organic thin-film transistors. *Adv. Mater. Technol.* **2017**, *2*, 1700167. [CrossRef]
5. Kim, J.T.; Lee, J.; Jang, S.; Yu, Z.; Park, J.; Jung, E.; Lee, S.; Song, M.H.; Whang, D.R.; Wu, S.; et al. Solution processable small molecules as efficient electron transport layers in organic optoelectronic devices. *J. Mater. Chem. A* **2020**, *8*, 13501–13508. [CrossRef]
6. Riede, M.; Lüssem, B.; Leo, K. Organic semiconductors. *Compr. Semicond. Sci. Technol.* **2011**, *4*, 448–507. [CrossRef]
7. Schwierz, F. Graphene Transistors: Status, Prospects, and Problems. *Proc. IEEE* **2013**, *101*, 1567–1584. [CrossRef]
8. Marconcini, P.; Macucci, M. Transport Simulation of Graphene Devices with a Generic Potential in the Presence of an Orthogonal Magnetic Field. *Nanomaterials* **2022**, *12*, 1087. [CrossRef]
9. Walker, A.B. Multiscale modeling of charge and energy transport in organic light-emitting diodes and photovoltaics. *Proc. IEEE* **2009**, *97*, 1587–1596. [CrossRef]
10. Chen, F.-C. Organic Semiconductors. *Encycl. Mod. Opt.* **2018**, *5*, 220–231. [CrossRef]
11. El-Saba, M. *Carrier Transport in Organic Semiconductors and Insulators*; IGI Global: Hershey, PA, USA, 2017. [CrossRef]
12. Kim, J.; Yasuda, T.; Yang, Y.; Adachi, C. Bifunctional Star-Burst Amorphous Molecular Materials for OLEDs: Achieving Highly Efficient Solid-State Luminescence and Carrier Transport Induced by Spontaneous Molecular Orientation. *Adv. Mater.* **2013**, *25*, 2666–2671. [CrossRef]
13. Choi, M.; Lee, H.-N. Light-emission and electricity-generation properties of photovoltaic organic light-emitting diodes with rubrene/dbp light-emission and electron-donating layers. *Int. J. Photoenergy* **2014**, *2014*, 361861. [CrossRef]
14. Saxena, K.; Mehta, D.; Rai, V.K.; Srivastava, R.; Chauhan, G.; Kamalasanan, M.; Jain, V. Studies on organic light-emitting diodes based on rubrene-doped zinc quinolate. *Phys. Status Solidi A* **2009**, *206*, 1660–1663. [CrossRef]
15. Weinberg-Wolf, J.R.; McNeil, L.E.; Liu, S.; Kloc, C. Evidence of low intermolecular coupling in rubrene single crystals by raman scattering. *J. Phys. Condens. Matter* **2007**, *19*, 276204. [CrossRef]
16. Sai, N.; Tiago, M.L.; Chelikowsky, J.R.; Reboredo, F.A. Optical spectra and exchange-correlation effects in molecular crystals. *Phys. Rev. B* **2008**, *77*, 161306. [CrossRef]
17. Wikipedia Contributors. Rubrene—Wikipedia, The Free Encyclopedia. 2021. Available online: https://en.wikipedia.org/w/index.php?title=Rubrene&oldid=1014340589 (accessed on 11 February 2022).

18. Reyes-Martinez, M.A.; Crosby, A.J.; Briseno, A.L. Rubrene crystal field-effect mobility modulation via conducting channel wrinkling. *Nat. Commun.* **2015**, *6*, 6948. [CrossRef]
19. Lin, K.; Wang, Y.; Chen, K.; Ho, C.; Yang, C.; Shen, J.; Chiu, K. Role of molecular conformations in rubrene polycrystalline films growth from vacuum deposition at various substrate temperatures. *Sci. Rep.* **2017**, *7*, 40824. [CrossRef]
20. Majewska, N.; Gazda, M.; Jendrzejewski, R.; Majumdar, S.; Sawczak, M.; Śliwiński, G. Organic semiconductor rubrene thin films deposited by pulsed laser evaporation of solidified solutions. In Proceedings of the SPIE 10453, Third International Conference on Applications of Optics and Photonics, Faro, Portugal, 8–12 May 2017; Volume 104532H. [CrossRef]
21. Zeng, X.; Zhang, D.; Duan, L.; Wang, L.; Dong, G.; Qiu, Y. Morphology and fluorescence spectra of rubrene single crystals grown by physical vapor transport. *Appl. Surf. Sci.* **2017**, *253*, 6047–6051. [CrossRef]
22. Reyes-Martinez, M.A.; Ramasubramaniam, A.; Briseno, A.L.; Crosby, A.J. The intrinsic mechanical properties of rubrene single crystals. *Adv. Mater.* **2012**, *24*, 5548–5552. [CrossRef]
23. Monkhorst, H.J.; Pack, J.D. Special points for brillouin-zone integrations. *Phys. Rev. B* **1976**, *13*, 5188–5192. [CrossRef]
24. Perdew, J.P.; Burke, K.; Ernzerhof, M. Generalized gradient approximation made simple. *Phys. Rev. Lett.* **1996**, *77*, 3865–3868. [CrossRef]
25. Perdew, J.P.; Chevary, J.A.; Vosko, S.H.; Jackson, K.A.; Pederson, M.R.; Singh, D.J.; Fiolhais, C. Atoms, molecules, solids, and surfaces: Applications of the generalized gradient approximation for exchange and correlation. *Phys. Rev. B* **1992**, *46*, 6671–6687. [CrossRef]
26. Perdew, J.P.; Ruzsinszky, A.; Csonka, G.I.; Vydrov, O.A.; Scuseria, G.E.; Constantin, L.A.; Zhou, X.; Burke, K. Restoring the density-gradient expansion for exchange in solids and surfaces. *Phys. Rev. Lett.* **2008**, *100*, 136406. [CrossRef]
27. Hohenberg, P.; Kohn, W. Inhomogeneous electron gas. *Phys. Rev.* **1964**, *136*, 864–871. [CrossRef]
28. Kohn, W.; Sham, L.J. Self-consistent equations including exchange and correlation effects. *Phys. Rev.* **1965**, *140*, 1133–1138. [CrossRef]
29. Giannozzi, P.; Andreussi, O.; Brumme, T.; Bunau, O.; Nardelli, M.B.; Calandra, M.; Car, R.; Cavazzoni, C.; Ceresoli, D.; Cococcioni, M. Advanced capabilities for materials modelling with quantum espresso. *J. Phys. Condens. Matter* **2017**, *29*, 465901. [CrossRef]
30. Giannozzi, P.; Baroni, S.; Bonini, N.; Calandra, M.; Car, R.; Cavazzoni, C.; Ceresoli, D.; Chiarotti, G.L.; Cococcioni, M.; Dabo, I. Quantum espresso: A modular and open-source software project for quantum simulations of materials. *J. Phys. Condens. Matter* **1964**, *21*, 395502. [CrossRef]
31. Vanderbilt, D. Soft self-consistent pseudopotentials in a generalized eigenvalue formalism. *Phys. Rev. B* **1990**, *41*, 7892–7895. [CrossRef]
32. Baroni, S.; De Gironcoli, S.; Dal Corso, A.; Giannozzi, P. Phonons and related crystal properties from density-functional perturbation theory. *Rev. Mod. Phys.* **2001**, *73*, 515–562. [CrossRef]
33. Louail, L.; Maouche, D.; Roumili, A.; Sahraoui, F.A. Calculation of elastic constants of 4d transition metals. *Mater. Lett.* **2004**, *58*, 2975–2978. [CrossRef]
34. Xing, G.; Sun, J.; Li, Y.; Fan, X.; Zheng, W.; Singh, D.J. Electronic fitness function for screening semiconductors as thermoelectric materials. *Phys. Rev. Mater.* **2017**, *1*, 065405. [CrossRef]
35. Jurchescu, O.D.; Meetsma, A.; Palstra, T.T.M. Low-temperature structure of rubrene single crystals grown by vapor transport. *Acta Crystallogr. B* **2006**, *62*, 330–334. [CrossRef]
36. Wang, D.; Tang, L.; Long, M.; Shuai, Z. First-principles investigation of organic semiconductors for thermoelectric applications. *J. Chem. Phys.* **2009**, *131*, 224704. [CrossRef] [PubMed]
37. Yanagisawa, S.; Morikawa, Y.; Schindlmayr, A. Homo band dispersion of crystalline rubrene: Effects of self-energy corrections within the gw approximation. *Phys. Rev. B* **2013**, *88*, 115438. [CrossRef]
38. Zhang, Y.; Manke, D.R.; Sharifzadeh, S.; Briseno, A.L.; Ramasubramaniam, A.; Koski, K.J. The elastic constants of rubrene determined by brillouin scattering and density functional theory. *Appl. Phys. Lett.* **2017**, *110*, 071903. [CrossRef]
39. Podzorov, V.; Menard, E.; Borissov, A.; Kiryukhin, V.; Rogers, J.A.; Gershenson, M.E. Intrinsic charge transport on the surface of organic semiconductors. *Phys. Rev. Lett* **2004**, *93*, 086602. [CrossRef]
40. Yamagishi, M.; Takeya, J.; Tominari, Y.; Nakazawa, Y.; Kuroda, T.; Ikehata, S.; Uno, M.; Nishikawa, T.; Kawase, T. High-mobility double-gate organic single-crystal transistors with organic crystal gate insulators. *Appl. Phys. Lett.* **2007**, *90*, 182117. [CrossRef]
41. Fumagalli, E.M. Growth and Physical Properties of Crystalline Rubrene. Ph.D. Thesis, Università Degli Studi di Milano-Bicocca, Milan, Italy, 2013.
42. Musa, A.; Gidado, A.S.; Mohammed, L.; Yunusa, K.; Suleiman, A. Molecular and Electronic Properties of Rubrene and Its Cyanide Derivative Using Density Functional Theory (DFT). *IOSR J. Appl. Phys.* **2019**, *11*, 10–18. [CrossRef]
43. Zhang, M.; Hua, Z.; Liu, W.; Liu, H.; He, S.; Zhu, C.; Zhu, Y. A dft study on the photoelectric properties of rubrene and its derivatives. *J. Mol. Model.* **2020**, *26*, 32. [CrossRef] [PubMed]
44. Missaoui, A.; Khabthani, J.J.; Laissardière, G.; Mayou, D. Two-dimensional electronic transport in rubrene: The impact of inter-chain coupling. *Entropy* **2019**, *21*, 233. [CrossRef] [PubMed]
45. Mukherjee, T.; Sinha, S.; Mukherjee, M. Electronic structure of twisted and planar rubrene molecules: A density functional study. *Phys. Chem. Chem. Phys.* **2018**, *20*, 18623–18629. [CrossRef]
46. Rang, Z.; Nathan, M.I.; Ruden, P.P.; Podzorov, V.; Gershenson, M.E.; Newman, C.R.; Frisbie, C.D. Hydrostatic pressure dependence of charge carrier transport in single-crystal rubrene devices. *Appl. Phys. Lett.* **2005**, *86*, 123501. [CrossRef]

47. Bisri, S.; Takenobu, T.; Takahashi, T.; Iwasa, Y. Electron transport in rubrene single-crystal transistors. *Appl. Phys. Lett.* **2010**, *96*, 183304. [CrossRef]
48. Fan, Q.; Wei, Q.; Yan, H.; Zhang, M.; Zhang, D.; Zhang, J. A new potential superhard phase of osn 2. *Acta Phys. Pol. A* **2014**, *126*, 740–747. [CrossRef]
49. Hill, R. The Elastic Behaviour of a Crystalline Aggregate. *Proc. Phys. Soc. Sect. A* **1952**, *A65*, 349. [CrossRef]
50. Pugh, S.F. XCII. relations between the elastic moduli and the plastic properties of polycrystalline pure metals. *Lond. Edinb. Dublin Philos. Mag. J. Sci.* **1954**, *45*, 823–843. [CrossRef]
51. Modeling hardness of polycrystalline materials and bulk metallic glasses. *Intermetallics* **2011**, *19*, 1275–1281. [CrossRef]
52. Machida, S.; Nakayama, Y.; Duhm, S.; Xin, Q.; Funakoshi, A.; Ogawa, N.; Ishii, H. Highest-occupied-molecular-orbital band dispersion of rubrene single crystals as observed by angle-resolved ultraviolet photoelectron spectroscopy. *Phys. Rev. Lett.* **2010**, *104*, 156401. [CrossRef]